PERGAMON

International Journal of Solids and Structures 38 (2001) 2653–2682

INTERNATIONAL JOURNAL OF SOLIDS and STRUCTURES

www.elsevier.com/locate/ijsolstr

On the initiation and growth of kink bands in fiber composites. Part II: analysis

T.J. Vogler, S.-Y. Hsu, S. Kyriakides *

Research Center for Mechanics of Solids, Structures and Materials, University of Texas at Austin, WRW 110/C0600, Austin, TX 78712-1085, USA

Received 17 January 2000; in revised form 20 April 2000

Abstract

Motivated by the experimental findings in Part I, the growth of a kink band in a uniaxial composite is investigated using two- and three-dimensional micromechanical models. The models include both a local and a global imperfection and were preloaded in compression and then sheared under displacement control. An inclined kink band initiates from the local imperfection and grows across the specimen. Similar results were obtained for pure compression loading. The simulated kink bands are quite similar to those observed experimentally; though, when J_2 plasticity is used to model the inelastic matrix, their inclination is lower than in experiments. The calculated band inclination is shown to be insensitive to many model parameters including imperfection characteristics, fiber diameter, volume fraction, and matrix yield stress. However, it is quite sensitive to the dilatancy of the matrix as demonstrated by the use of the Drucker–Prager constitutive model for the matrix. It was found that the ability of the matrix to deform in the direction transverse to the fibers plays an important role in allowing larger, more realistic kink band inclinations to be obtained.

Keywords: Composites; Compression; Kink band initiation

1. Introduction

The experimental results in Part I of this series provide direct information on how inclined kink bands grow in aligned fiber composites. In addition, the geometric characteristics of growing kink bands were accurately established. In Part II, we extend the 2-D and 3-D micromechanical models of Kyriakides et al. (1995) [1] and Hsu et al. (1998)[1] and use them to simulate compression-shear tests like the ones discussed in Part I. It will be shown that, as was the case experimentally, this type of loading allows controlled growth of kink bands. As has been established in past studies, failure of such composites is governed by the interaction of geometric imperfections in the form of fiber misalignment with the nonlinear shear response of the

* Corresponding author. Fax: +1-512-471-5500.
E-mail address: skk@mail.utexas.edu (S. Kyriakides).

[1] Refers to figures and references in Part I.

0020-7683/01/$ - see front matter
PII: S0020-7683(00)00175-X

composites. Micromechanical models analyzed in the references mentioned had imperfections which were generally global. In the present effort, in order to help initiate kink bands locally, local imperfections are included in the models as described below.

2. Micromechanical models

The general characteristics of the 2-D and 3-D models are the same as those described in the studies of pure compression in the two references mentioned above. In Vogler et al. (2000),[1] the two models were modified in order to enable simulation of failure under combined compression and shear. Those modifications are also adopted here with some additional changes, which will enable us to simulate local initiation and growth of kink bands. The general characteristics of the models are as follows. In the 2-D model, the composite is idealized as an alternating array of fiber and matrix layers as shown in Fig. 1. The fiber thickness (h) and the fiber spacing are chosen so as to end up with the required fiber volume fraction (v_f) of the composite. In the 3-D model, the fibers are circular with diameter h and are distributed in a hexagonal arrangement in the matrix as shown in Fig. 2. The spacing of the fibers (c) is related to the fiber diameter and volume fraction through the relation:

$$c = h\sqrt{\frac{\pi\sqrt{3}}{6v_f}}. \tag{1}$$

In both types of models, unless otherwise stated, $h = 7$ μm and $v_f = 60\%$.

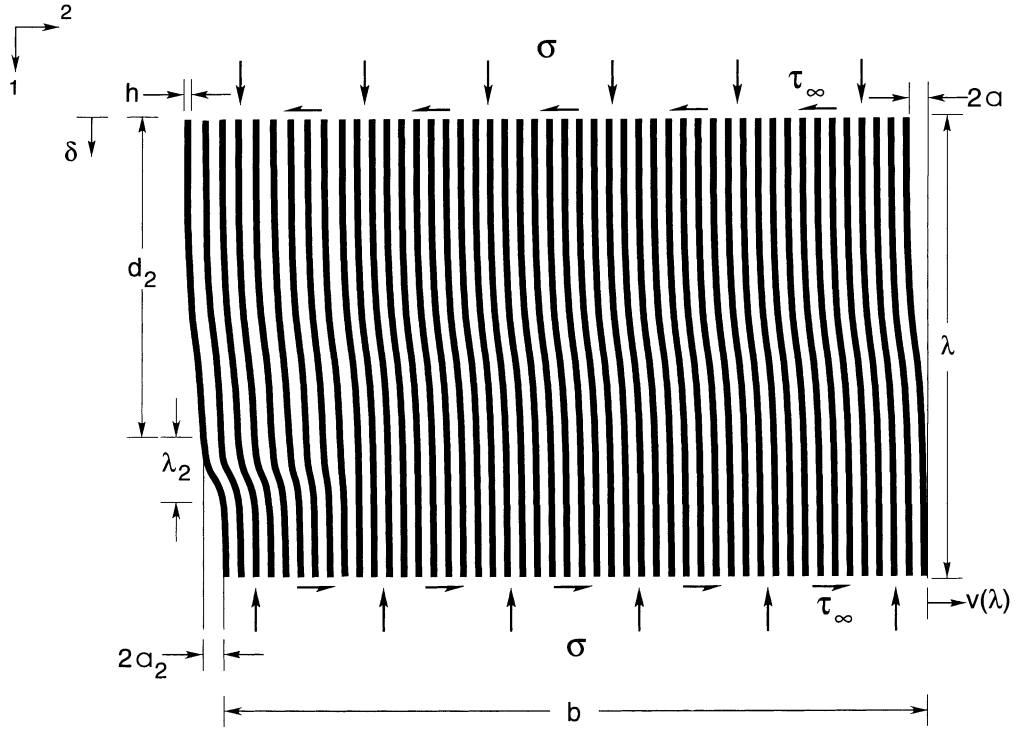

Fig. 1. Geometry of 2-D composite micromodel with global and local fiber imperfections shown loaded in compression and shear.

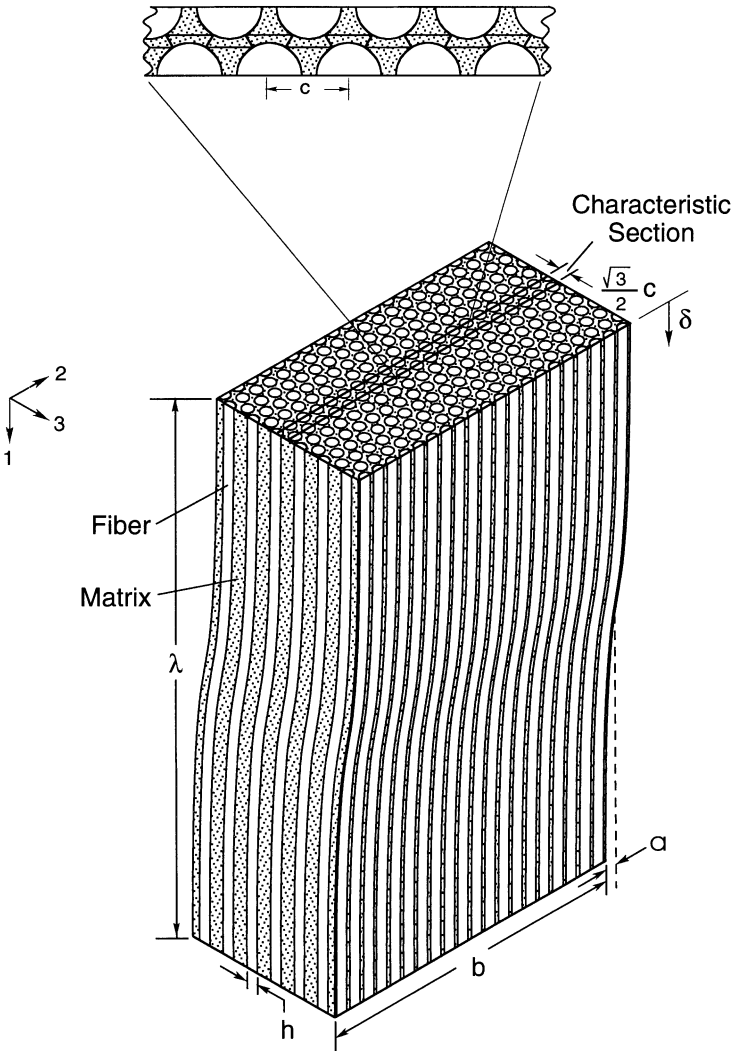

Fig. 2. Geometry of composite idealized as an hexagonal array of fibers for use in the 3-D micromodel.

Two imperfections are included in the models. The first, referred to as the *global imperfection* is a sinusoidal waviness of the fibers along the x_1-direction with amplitude a and half wavelength λ. This imperfection is uniform across the width of the microsections and is expressed as

$$v_o = -a\cos\frac{\pi x_1}{\lambda}. \tag{2}$$

A *local imperfection* is added to a strip of N fibers at the free left side edge to initiate a kink band. This imperfection consists of a sine wave of half wavelength λ_2, which begins at a distance d_2 from the top of the microsection. Its amplitude is a_2 at $x_2 = 0$ but decays linearly over the N fibers it affects. The local imperfection is expressed as

$$v_{o2} = \begin{cases} -2a_2\left(1 - \frac{i-1}{N}\right), & 0 \leqslant x_1 < d_2, \\ -a_2\left(1 - \frac{i-1}{N}\right)\left[1 + \cos\left(\frac{\pi(x_1 - d_2)}{\lambda_2}\right)\right], & d_2 \leqslant x_1 \leqslant d_2 + \lambda_2, \\ 0, & d_2 + \lambda_2 < x_1 \leqslant \lambda, \end{cases} \tag{3}$$

where $1 \leqslant i \leqslant N$ is the fiber number counted from the left edge. Unless otherwise stated $N = 12$ both for 2-D and 3-D simulations. (Note that in the region of influence of the local imperfection, v_f is somewhat less than 60%.)

In the 3-D models, periodicity of the microstructure in the x_3-direction allows consideration of just the representative slice of the material shown in Fig. 2 of thickness $\sqrt{3}c/2$. The characteristic slice is shown in Fig. 3 without the local imperfection. The two lateral surfaces of the slice are assumed to have zero displacement in the x_3-direction.

For pure compression calculations, Kyriakides et al. (1995)[1] and Hsu et al. (1998)[1] invoked periodicity in the x_1-direction. Thus, their models were limited to heights of either λ or $\lambda/2$. For the present problem, periodicity no longer exists due to the addition of shear. Instead, microsections one-half period long and width b defined by the number of fibers n_f are used. In both type models, the fibers and matrix are discretized with finite elements. Details about the discretizations can be found in Kyriakides et al. (1995)[1] and Hsu et al. (1998)[1].

Axial loading is such that the top and bottom surfaces of the microsections in Figs. 1 and 3 remain plane. The top of each model ($x_1 = 0$) is fixed in the x_1-direction. A vertical force is then prescribed incrementally at the bottom ($x_1 = \lambda$). In simulations of shear under constant axial stress ($\sigma \to \gamma$ loading path), the initial axial loading is applied as just described to allow for Poisson expansion. The model is then sheared by fixing the top surface and prescribing the same displacement in the x_2-direction to all nodes at the bottom end of the model. Some redistribution of axial stresses may occur during the shearing, affecting somewhat the constraint at the ends of the fibers. However, this effect was found to be limited to narrow regions at the ends of the model, and the results were generally not sensitive to the details of the boundary conditions imposed at the top and bottom surfaces.

The left and right sides of both models are free. As in the experiments, this causes some nonuniformity in the axial stress as well as in the shear stress as discussed in Vogler et al. (2000)[1]. A large aspect ratio will reduce the effect of the nonuniformities, but too large an aspect ratio can inhibit the development of a kink band for the reasons discussed in the next section. To alleviate the last difficulty, the local imperfection is placed at a distance d_2 from the top rather than at the center of the model as shown in Fig. 1.

Key components of these models are the constitutive laws adopted for the fibers and matrix. As in the past, we assume the fibers to be isotropic and linearly elastic with the properties given in Table 1 (Panel A). For the majority of calculations, the matrix is modeled as a finitely deforming J_2-type elasto-plastic solid which hardens isotropically. The properties of the matrix in each model were extracted from a torsion test on a filament wound thin-walled tube of this material as follows. In each case, a representative micromodel was loaded under pure shear (layered for 2-D, hexagonal fiber array in matrix for 3-D). The fibers were assigned the properties in Table 1 (Panel A). The matrix properties were calculated iteratively such that each model composite matches the measured shear response (Hsu et al., 1998[1]). For strains higher than 9% in the 2-D case and 11% in the 3-D case, the stress–strain responses are assumed to be perfectly plastic. The two matrix stress–strain responses established in this manner are compared with results from a tension test on neat PEEK in Fig. 4(a). The matrix properties used for the 2-D model are stiffer than the neat properties for all strain levels. Those used for the 3-D models are similar to neat properties at lower strains (<3%) but are stiffer for higher strains. Fig 4(b) shows a comparison of the measured shear response and that from the 2-D model using the extracted stress–strain response. Agreement with experimental data is quite good. The one obtained from the 3-D model is very similar to this and will not be shown.

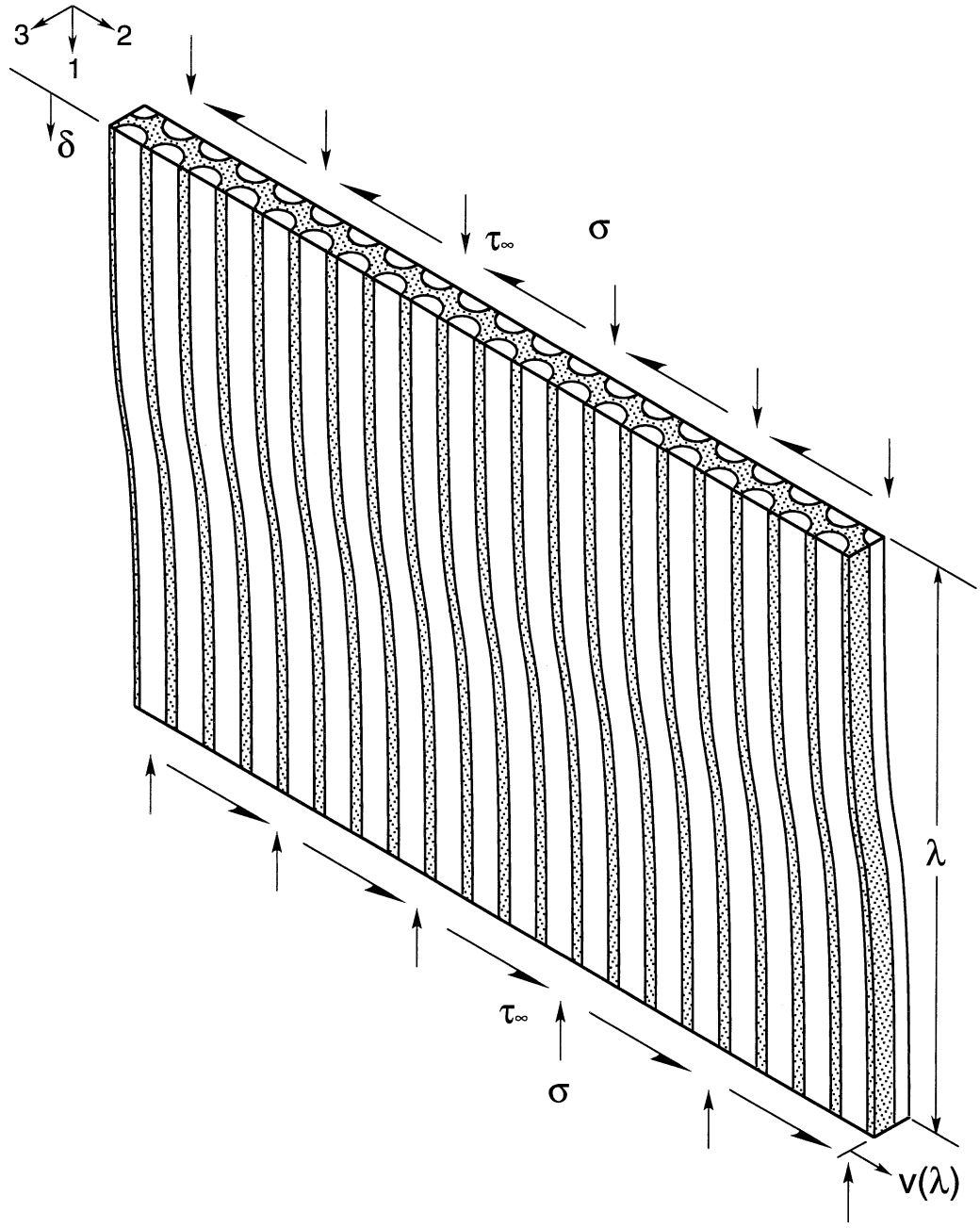

Fig. 3. Characteristic section of the idealized composite used for the 3-D micromodel loaded in compression and shear.

The inelastic behavior of PEEK is complex. Though J_2-type plasticity is sufficient for the relatively limited nonlinearity involved up to the onset of failure, it does not capture all of the subtleties of the composite's behavior in the post-failure regime. Most notable is the inability of J_2-type plasticity to model

Table 1
Material properties of the composite and its constituents

Panel A: APC-2/AS4 composite					
E_{11} msi (GPa)	E_{22} msi (GPa)	G_{12} msi (GPa)	ν_{12}	v_f	
18.62 (128)	1.533 (10.57)	0.84 (5.79)	0.3	60%	
Panel B: AS4 fibers					
E_f msi (GPa)				ν_f	
31.0 (214)				0.263	
Panel C: APC-2 (PEEK) matrix					
2-D Models			3-D Model		
E_m ksi (GPa)	σ_{om} ksi (MPa)	ν_m	E_m ksi (GPa)	σ_{om}ksi (MPa)	ν_m
893 (6.14)	11.9 (82.1)	0.356	594 (4.10)	9.5 (65.5)	0.356

the pressure sensitivity of this polymeric matrix. It is well known that the nonlinear behavior of many polymers, including PEEK, is sensitive to imposed hydrostatic pressure (Christiansen et al., 1971; Santore et al., 1991; Sauer et al., 1973; Spitzig and Richmond, 1979; see also Fig. 5 of Hsu et al. (1999b)). A second restriction of J_2-type plasticity is its assumption of zero plastic dilatancy. While this assumption is justified for many metals, it is known that polymers can exhibit inelastic dilatation (same references). It will be shown that these two factors can play a role in the characteristics of kink bands during their initiation. To address to some degree these deficiencies, the Drucker and Prager (D–P) (1952) plasticity model is also implemented. The yield function is of the form

$$f = \sqrt{3J_2} + \alpha I_1 = k, \tag{4a}$$

where α and k are constants and

$$I_1 = \sigma_{kk}, \qquad J_2 = \tfrac{1}{2}s_{ij}s_{ij} \quad \text{and} \quad s_{ij} = \sigma_{ij} - \tfrac{1}{3}\sigma_{kk}\delta_{ij}. \tag{4b}$$

A variant of this model has been used previously in Hsu et al. (1999b). Here, the rate-independent *associative* version is used with $\alpha = 0.1415$. This value was found by Hsu et al. to allow the model to reproduce aspects of the composites' nonlinear behavior under shear and transverse compression. The in situ matrix has the same shear response as for the J_2-type model (Fig. 4b). We first note that Christiansen et al. (1971), Sauer et al. (1973), Spitzig and Richmond (1979) and others have shown that yield function (4) with $0.05 < \alpha < 0.2$ captures the pressure sensitivity of the yielding of several polymers (amorphous and crystalline). Evidence that polymers dilate under shear has also been published but is more sketchy (Pixa et al., 1988; Santore et al., 1991). At the same time, we know from Hsu et al. (1999b) that this model does not provide an adequately broad and accurate description of the composite's nonlinearity. We adopt it because it will allow us to demonstrate the sensitivity of aspects of the initiation of kink bands to variables not available in J_2 plasticity.

3. Predictions

The two models are now used to study the details of the initiation of kink bands and the way they grow across specimens. The 2-D microsections analyzed have a half wavelength of $\lambda = 143h$ and are 150 fibers

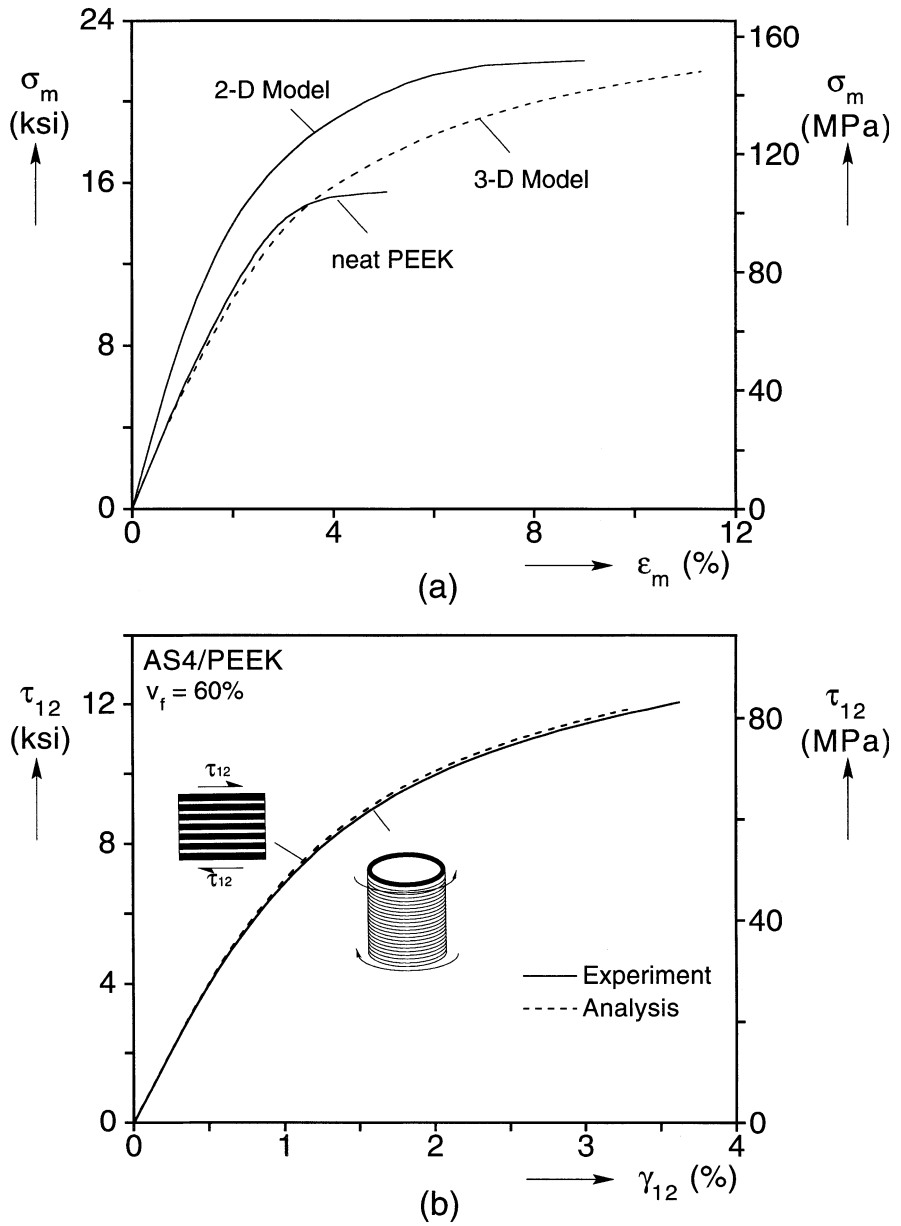

Fig. 4. (a) Comparison of matrix properties used in the 2-D and 3-D micromodels with neat PEEK data. (b) Experimental shear response and response from 2-D model.

wide which corresponds to a physical width of $250h$. The 3-D models have a half wavelength of $\lambda = 112h$ and are 120 fibers wide which corresponds to a physical width of $148h$. These imply respective micromodel aspect ratios (b/λ) of approximately 1.75 and 1.32. All geometric parameters of the models are listed in Table 2.

Table 2
Geometric parameters for standard 2-D and 3-D micromechanical models

Model type	v_f	n_f	λ/h	a/h	λ_2/h	a_2/h	N	d_2/h
2-D	0.60	150	143	0.5	12	1	12	95
3-D	0.60	120	112.5	0.5	12	1	12	69

3.1. Shearing under constant compressive stress

We first consider micromodels which are sheared under a prescribed compressive stress (σ–γ loading path) much like in the experiments described in Part I.

3.1.1. 2-D model

The 2-D microsection is first compressed to an average stress of 90 ksi (621 MPa) as shown from I to II in Fig. 5a. The model is then sheared in displacement control while the axial stress is kept constant (II to III). The τ–γ response obtained is shown in Fig. 5b. As shearing progresses, the shear stress increases, becoming quite nonlinear at levels beyond 4 ksi (27 MPa). Accompanying the shearing is a corresponding shortening of the model as seen from II to III in Fig. 5a. Eventually, the shear deformation in the vicinity of the local imperfection becomes sufficiently large for the axial stress to locally buckle the fibers initiating the kink band. Concurrently, a limit load is reached at a shear stress of 7.13 ksi (49.2 MPa) followed by a gradual drop in the stress required to further shear the specimen (note qualitative resemblance of results with experimental results in Fig. 3[1]). The transverse displacement ($v(\lambda)$ in Fig. 1) must, however, increase for further deformation to take place. It is this characteristic that makes the process controllable.

Fig. 6 shows five deformed configurations of the model at points indicated by • on the response in Fig. 5b. They are truncated in the x_1-direction (only 43% of the height is shown) for better clarity of the growth of the zone of localized deformation. The edges of the band are delineated with dots marking the boundaries of where the equivalent plastic strain in the matrix has reached a value of 8%. (This value was found to correlate quite well with the location of the highest curvature of the fibers, the criterion we used in the past for the same purpose.) Using this criterion, in Fig. 7a we plot the width (w, see Fig. 5[1]) of the growing band as a function of x_2. The rotation of the fibers inside the band (ϕ, see Fig. 5[1]) is plotted against x_2 in Fig. 7b.

In configuration ①, close to the limit load, the mesh is quite deformed in shear but, with the onset of localized fiber buckling on the very left of the model, a gradient in fiber rotation is seen to develop. For this configuration, the region of high strain is relatively small and lies inside the local imperfection.

In configuration ②, the zone of highly bent fibers grows both in width as well as length and spreads to the material outside the local imperfection. The growth of w and ϕ confirm this trend also. Concurrently the average shear stress drops. An inclined band of bent fibers with an inclination of about 5.5° has now clearly emerged. Due to the local bending rigidity of the microstructure, for compatibility of deformation, localized bending tends to propagate in the form of a narrow band quite a distance away (this resembles Budiansky's (1983)[1] "characteristic directions" but in a highly plasticized material instead of the elastic composite he assumed).

In configuration ③, the band has grown further and begins to resemble the experimentally observed kink band in Fig. 6[1]. The width of the band continues to grow and so does the rotation of the fibers inside it, while the gradient from left to right of both remains. The band continues to grow in ④ and in ⑤ as it reaches the right side of the model. At this stage, the inclination of the band is 5.7° and its

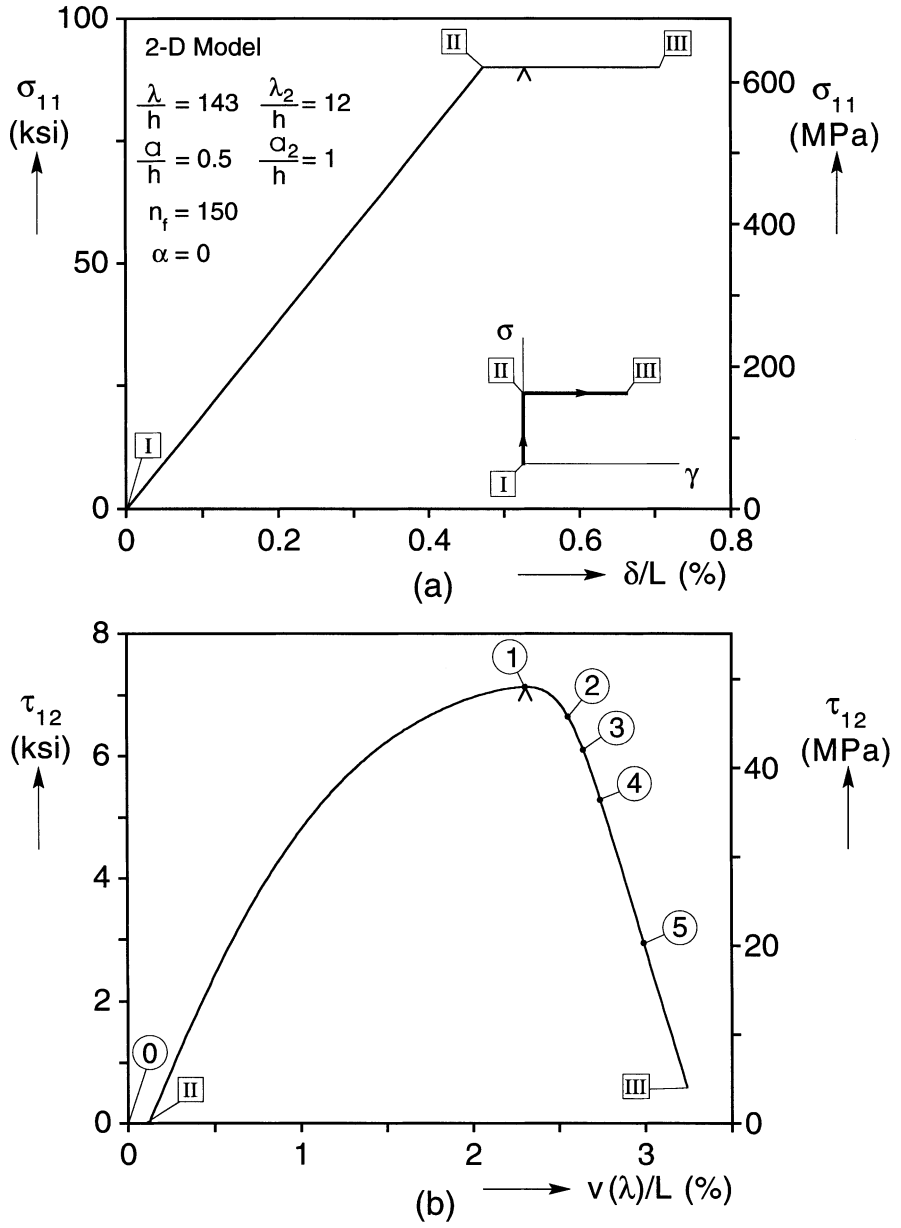

Fig. 5. Results from the 2-D model: (a) Axial stress-end shortening and (b) shear–stress horizontal displacement responses.

width varies between 17h on the left and 18h on the right (the values of β quoted are based on a linear fit through the points of maximum fiber rotation inside the band). The fiber rotation inside the band varies from approximately 8.5° on the left to 7.2° on the right. By configuration ⑤, the average shear stress has dropped down to nearly 3 ksi (20.7 MPa). Continued deformation beyond this point is possible. It will result in rotation and broadening of the band as seen in Kyriakides et al. (1995)[1] and Hsu et al. (1998,[1] 1999a). However, the axial stress required for this to happen drops below the 90 ksi

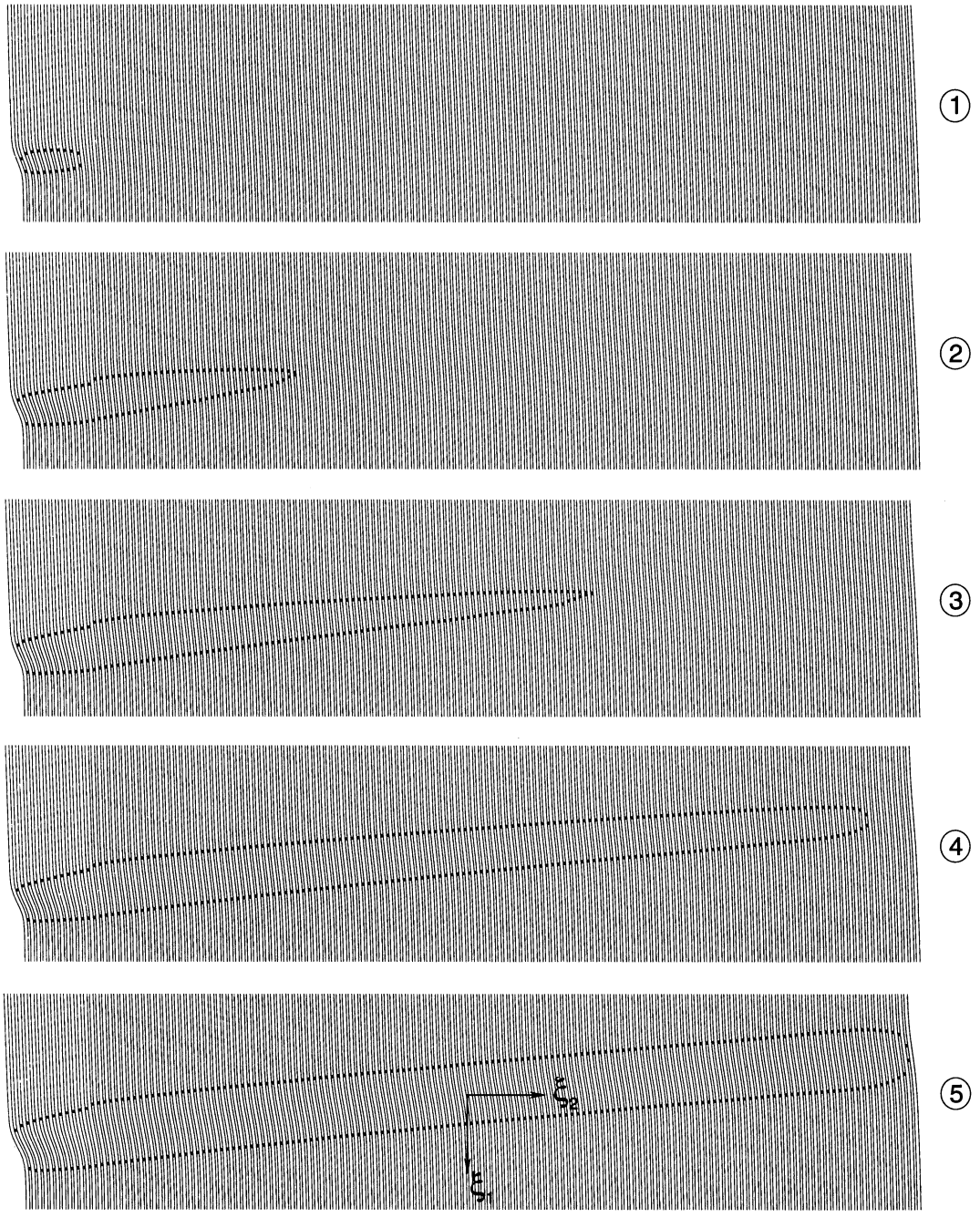

Fig. 6. Truncated deformed configurations of the 2-D model showing growth of kink band across it. Configurations correspond to points marked on τ_{12}–$\nu(\lambda)$ response in Fig. 5b.

level, and thus an alternate loading scheme needs to be implemented for the response to be followed much further.

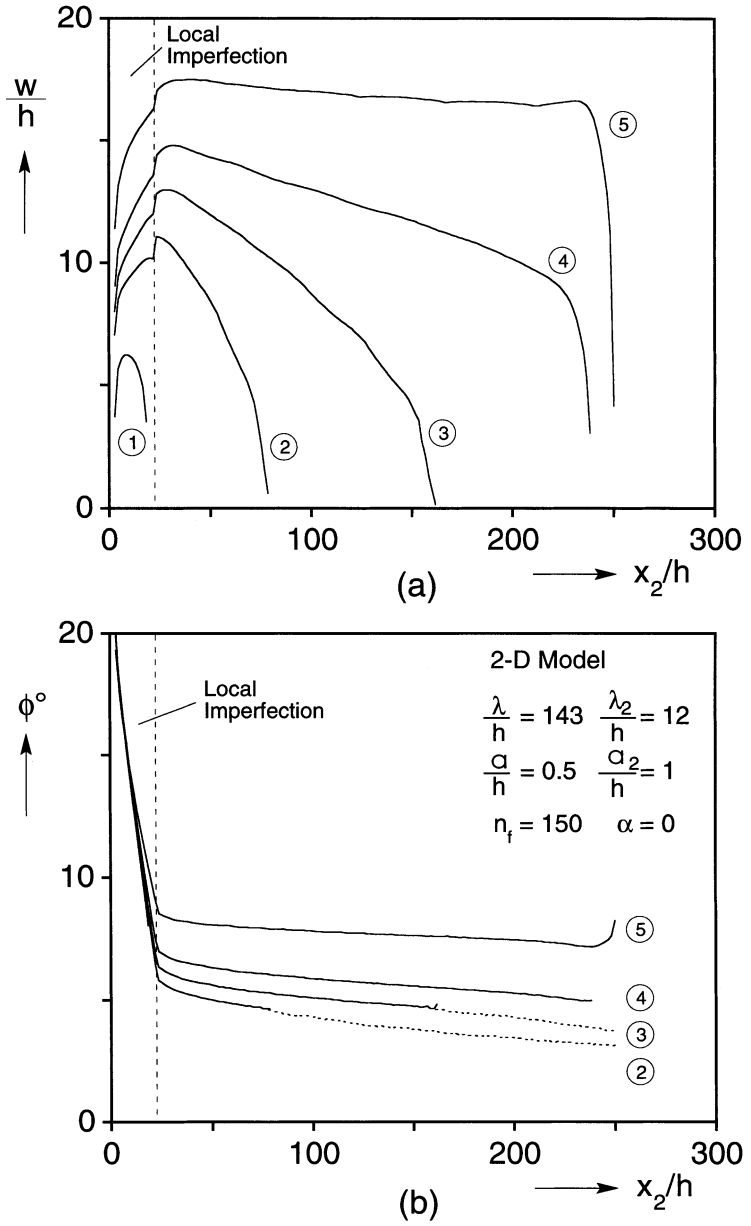

Fig. 7. Characteristics of kink band at points marked on τ_{12}–$v(\lambda)$ response in Fig. 5b: (a) bandwidth and (b) fiber rotation.

3.1.2. 3-D model

The same calculation was repeated for the 3-D model with the basic characteristics given in Table 2. This is a much larger calculation, and, for computational efficiency, the size of the micromodel was selected to be a bit smaller. The calculated responses are shown in Fig. 8. Five deformed configurations (truncated in the x_1-direction) corresponding to the points marked by solid bullets on the response in Fig. 8b are shown in Fig. 9. The edges of the band are identified once more by solid dots marking points in the matrix (central

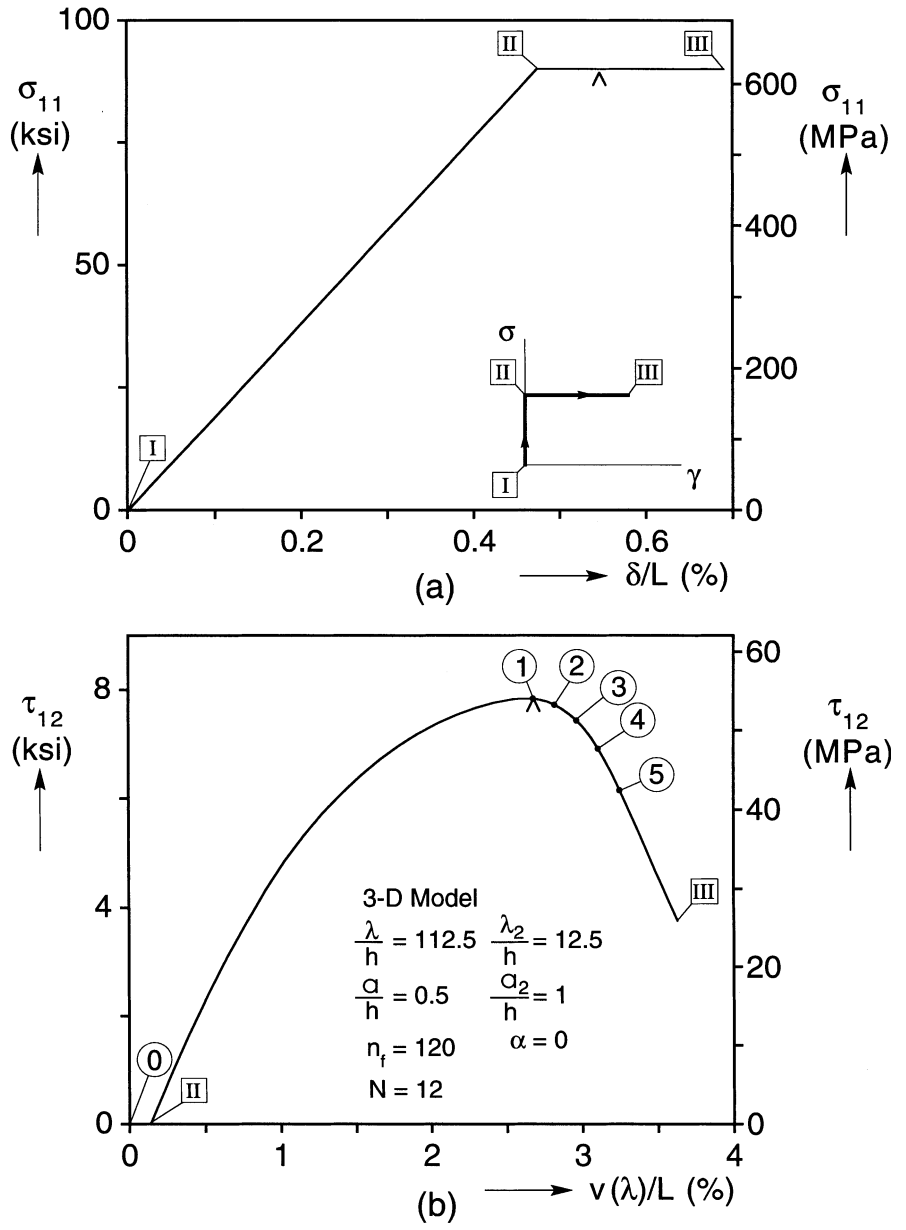

Fig. 8. Results from the 3-D model: (a) axial stress-end shortening and (b) shear–stress horizontal displacement responses.

row of elements between fibers – see inset in Fig. 2), which have reached equivalent plastic strains of 6%. (This lower value of strain was chosen because the central row of elements does not include the zones of highest stress levels seen by the matrix – see Fig. 14a in Hsu et al. (1999b).) The evolution of the kink band across the microsection is similar to what was observed in the 2-D micromodel. The band width and fiber rotation inside the band for the five configurations are plotted in Fig. 10. The main characteristics of the response and of the evolution of the band are very similar to the corresponding 2-D results. The critical

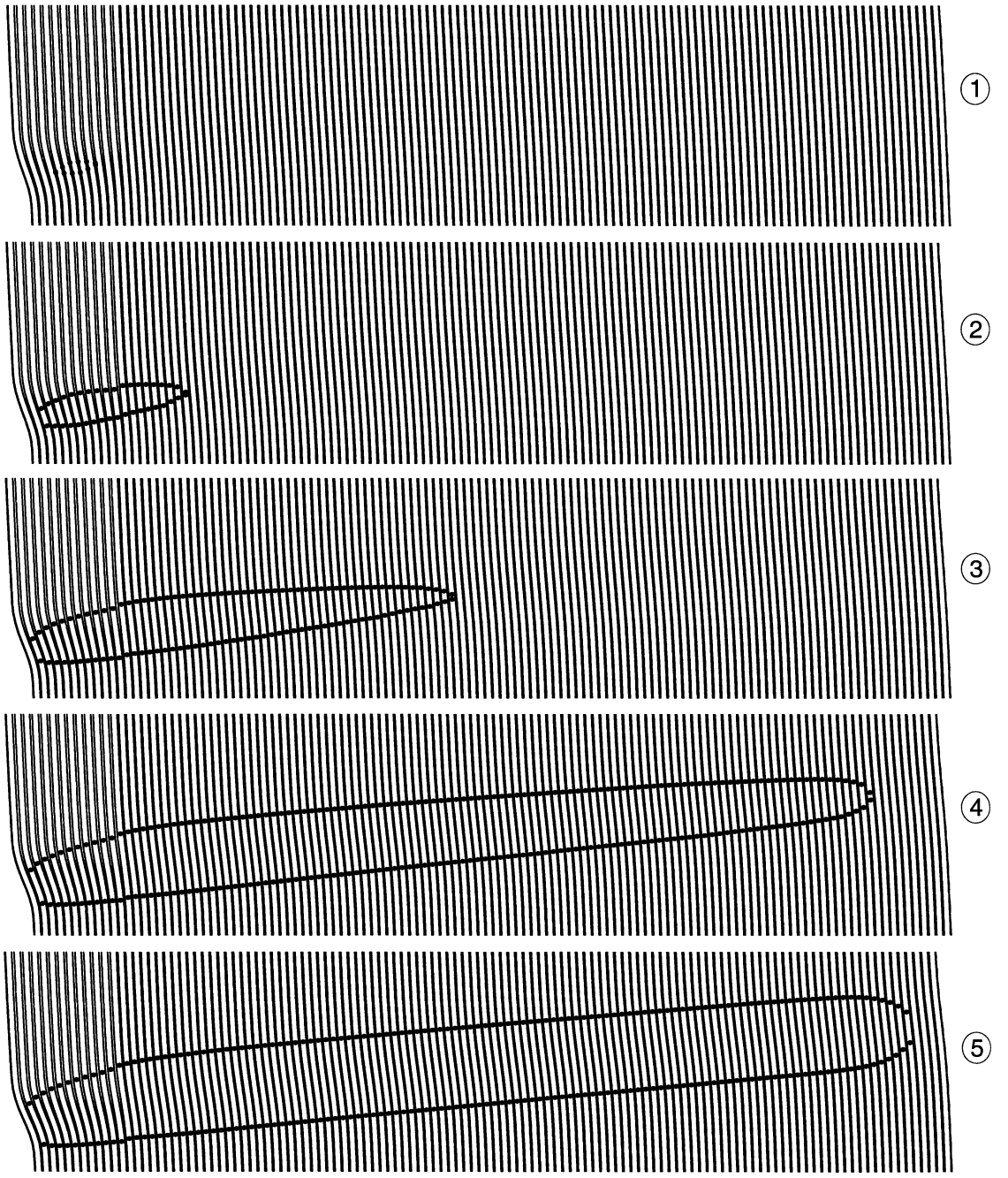

Fig. 9. Truncated deformed configurations of the 3-D model showing growth of kink band across it. Configurations correspond to points marked in τ_{12}–$v(\lambda)$ response in Fig. 8b.

shear stress and the characteristics of the fully developed band (configuration ⑤) are compared to those of the 2-D case in Table 3. Once again, the calculated band inclination is of the order of 50% of measured values.

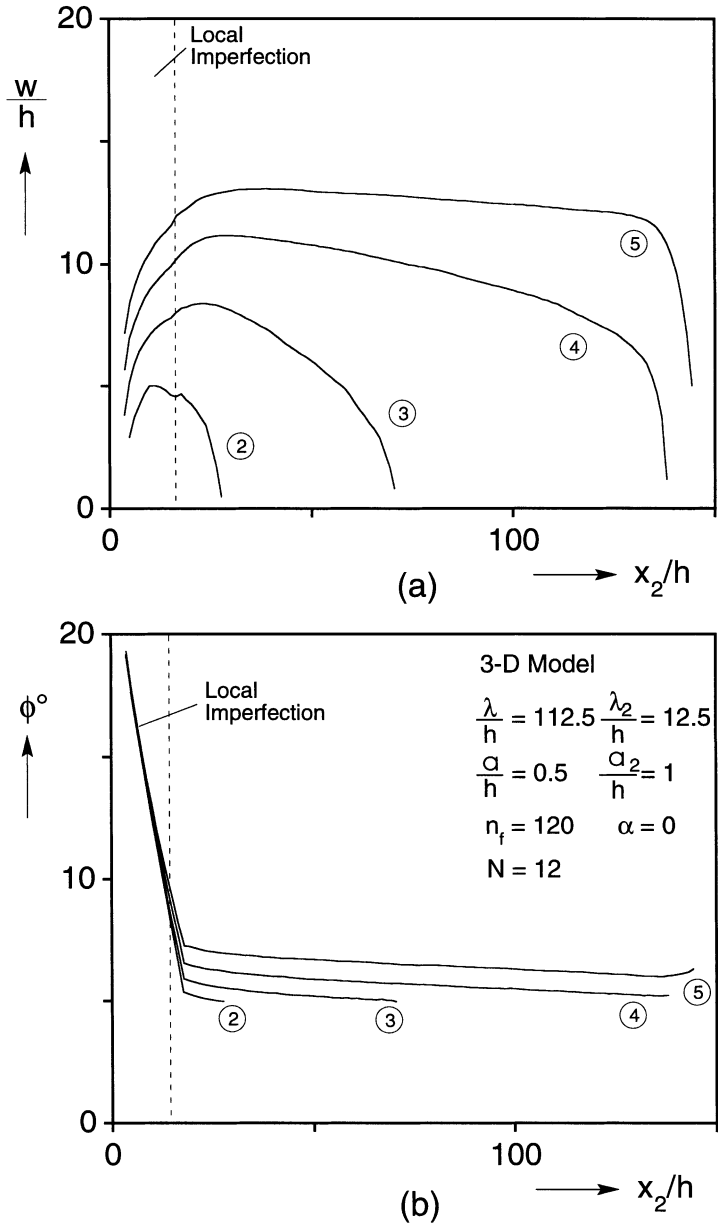

Fig. 10. Characteristics of kink band at points marked on τ_{12}–$\nu(\lambda)$ response in Fig. 8b: (a) bandwidth and (b) fiber rotation.

3.2. Pure compression

As mentioned in Part I, the initiation of a kink band under pure compression and its evolution across a finite size specimen occur dynamically and, as a result, are difficult to capture experimentally. Once a kink band is initiated, the load drops precipitously and energy from the surrounding material that unloads feeds into the deforming zone. The catastrophic nature of the post-failure response has been demonstrated in

Table 3
Critical stresses and kink band characteristics for 2-D and 3-D microsections loaded via the σ–γ loading path

Model type	α	σ ksi (MPa)	τ_C ksi (MPa)	ϕ°	β°	w/h
2-D PS	0	90 (621)	7.13 (49.2)	8	5.4	16
2-D PSN	0	90 (621)	7.19 (49.6)	7	4.7	16
3-D	0	90 (621)	7.84 (54.1)	6.5	5.6	13
2-D PS	0.1415	90 (621)	7.20 (49.7)	8	10.2	16
2-D PSN	0.1415	90 (621)	7.77 (53.6)	*	14.6	*
3-D	0.1415	90 (621)	8.62 (59.4)	7	17.3	13

calculations involving compression of finite size specimens with various types of fiber imperfections (Kyriakides et al., 1995)[1]. The axial stress-shortening response was found to exhibit a limit load associated with the onset of failure. Subsequently, the response traced a cusp-like trajectory, a strong indication that it cannot be followed by normal means of displacement control. Because of the finite width of these models and the global nature of the imperfections used, the kink bands formed were essentially uniform across the specimen width. They started with zero inclination and, as fiber rotation grew, they became increasingly more inclined.

An inclined kink band can be initiated by adding a large enough local imperfection to such micromodels. We use the same 2-D model used above with the same global imperfection. The local imperfection has the same amplitude and length but it is extended to affect a strip 25 fibers wide. The initiation process here is a much more unstable event and a more extensive local imperfection was necessary for proper initiation of a kink band. The specimen is compressed such that the top and bottom surfaces remain flat. The calculated σ–δ response is shown in Fig. 11. It is similar to the ones calculated before for such specimens with uniform imperfections. However, because of the presence of local imperfection on the left free edge of the specimen, failure is initiated at 192 ksi (1.32 GPa) about 30% lower than the critical load for the same case in the absence of the local imperfection. In the vicinity of the local imperfection, the highly rotated fibers cause earlier yielding of the matrix. An inclined kink band is initiated growing from left to right as seen in the sequence of deformed configurations (truncated) in Fig. 12. The characteristics of the growing band are similar to those discussed above for the case of shearing under constant compression (Fig. 13). The inclination of the band in configurations ④ and ⑤ is around 4.8° and the width of the fully grown band is around 15h, both of which are very close to the corresponding values in Fig. 7. The fiber rotation inside the band is also of the same order of magnitude. Continued compression past ⑤ results in an increase in the fiber rotation and in the inclination of the band.

In summary, the larger initial fiber rotation in the local imperfection causes earlier plastification of the matrix, and this leads to localized buckling of the fibers. This is associated with the overall limit load in the response. The localized buckling grows into an inclined band, which is preceded by an inclined characteristic. The tip of the growing band provides a destabilizing shear deformation to the material in front of it so that the band can grow. When fully developed, the band has an inclination of approximately 4.8° and a width of approximately 15h. To connect with our past work on models with essentially uniform or more global imperfections, the gradual development of a band in such models, starting from zero inclination at the limit load and growing to an inclined band with a distinct width, can be viewed as the sequence of events that take place in the transition zone in the tip of the growing band.

3.3. Band characteristics

The inclinations of the bands initiated in the models presented are in general smaller than the measured values. The predicted width of fully developed kink bands is closer to measured values but also somewhat smaller. These differences are partly due to the two-dimensional nature of the idealized composite but, as we

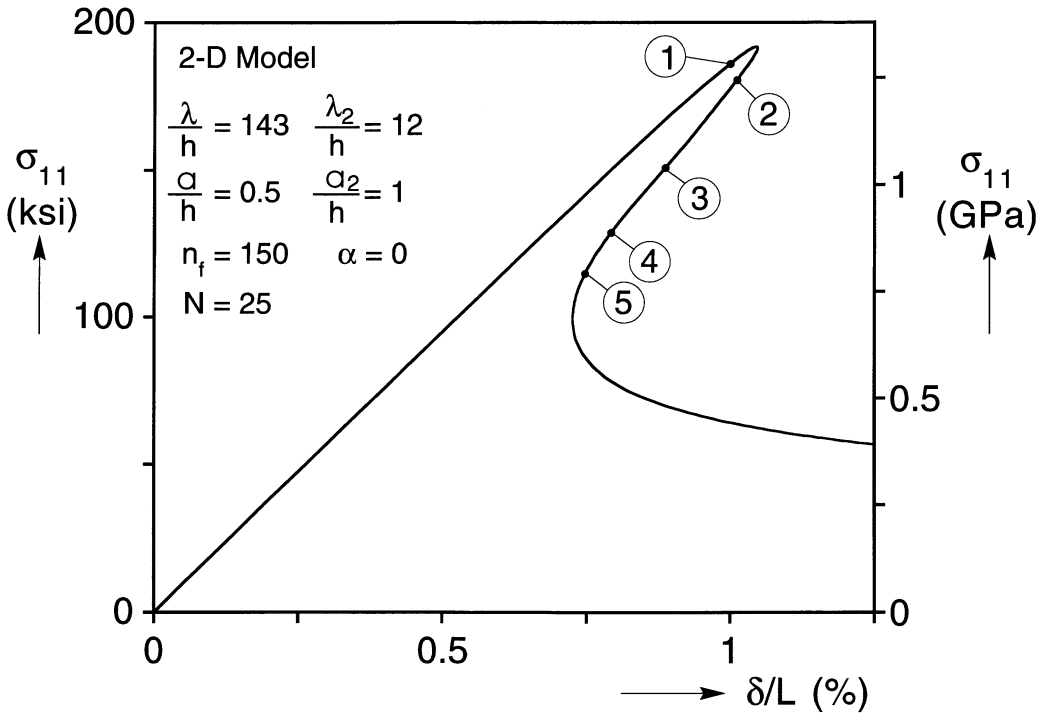

Fig. 11. Axial stress-end displacement response of the 2-D model loaded in pure compression.

will see, are also due to other factors such as limitations of J_2 plasticity. A parametric study was undertaken to explore this issue. The composite parameters varied were the fiber volume fraction (v_f), the matrix yield stress (σ_{om}) and the fiber diameter (h). The imperfection parameters varied were the amplitude (a_2), wavelength (λ_2) and width (N) of the local imperfection, and the amplitude of the global imperfection (a). The main model parameter examined was its width defined by the number of fibers included (n_f). In addition, results from plane stress and plane strain models were compared. The main matrix constitutive issue examined was sensitivity of the problem to pressure sensitivity and inelastic dilatancy of the material. These are examined by switching to the Drucker–Prager model ($\alpha \neq 0$ in Eq. (4a)). The vehicle of the parametric study is the shear-under compression test described in Part I. The model discussed under Section 3.1.1 with the parameter listed in the first row of Tables 2 and 4 will be considered as the base case. The major results from this case are also listed in this table. Each parameter is varied individually while all other parameters are assigned the values of the base case.

3.3.1. Composite parameters

The composite variable considered first is the fiber volume fraction. The base case has $v_f = 60\%$. Thus, in addition, we analyzed models with v_f of 50% and 70%. In order to maintain the width of the microsection constant, the number of fibers was respectively increased and decreased appropriately for the two cases (see n_f in Table 4). Changing the fiber volume fraction results in a change in the shear response of the material, which has direct implications on the failure stress. In the present setting, we kept the initial compressive stress at the level of 90 ksi (621 MPa). Thus, the change in shear response results in a reduction of the critical shear stress for $v_f = 50\%$ to 6.35 ksi (43.8 MPa) and an increase for $v_f = 70\%$ to 7.96 ksi (54.9 MPa).

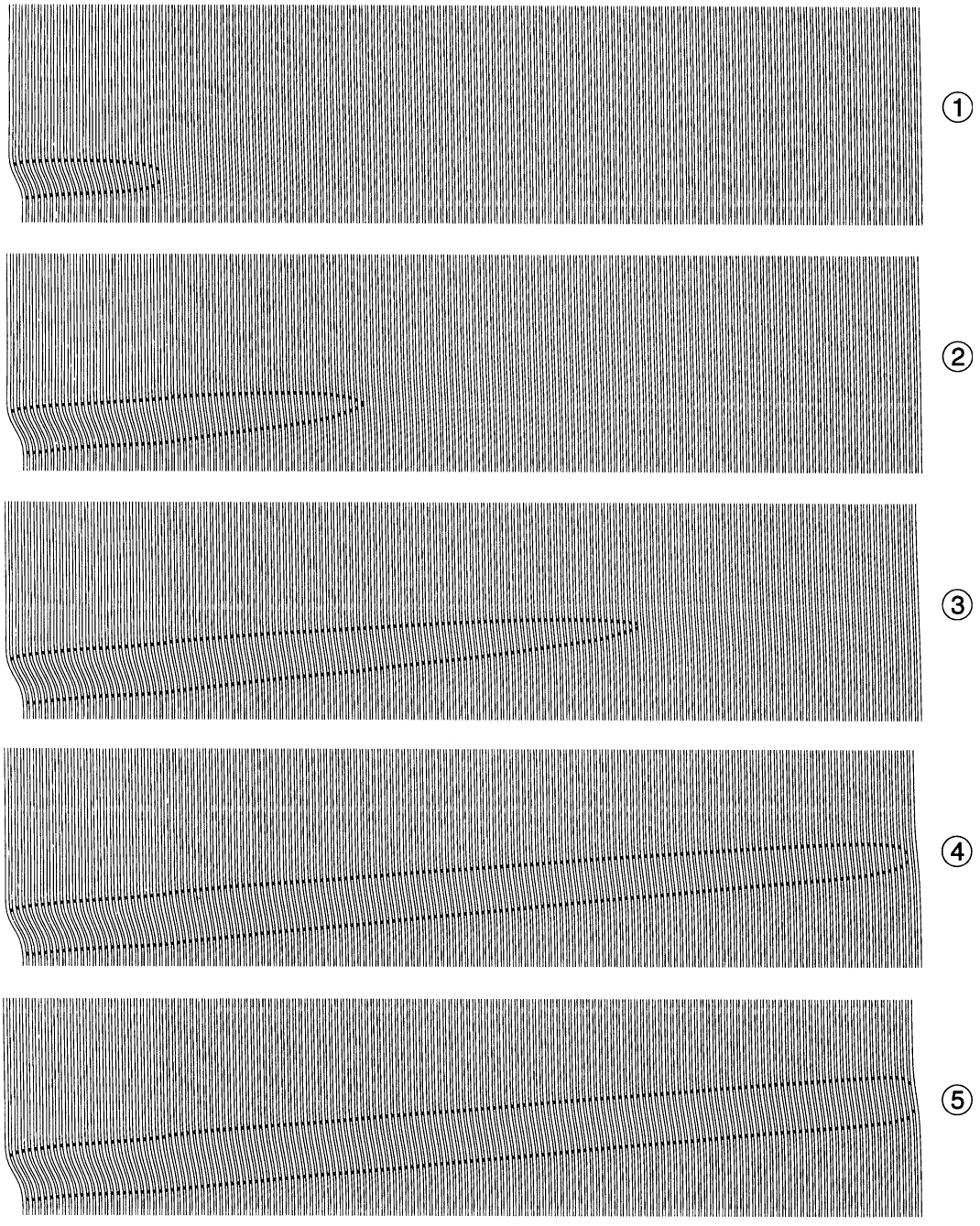

Fig. 12. Truncated deformed configurations of the 2-D model showing growth of kink band across it. Configurations correspond to points marked on σ_{11}–δ response in Fig. 11.

Fully developed kink bands for the three cases are compared in Fig. 14. The band inclination did not change significantly (Table 4) while its width grew somewhat for the stiffer material ($w \approx 18h$) and decreased

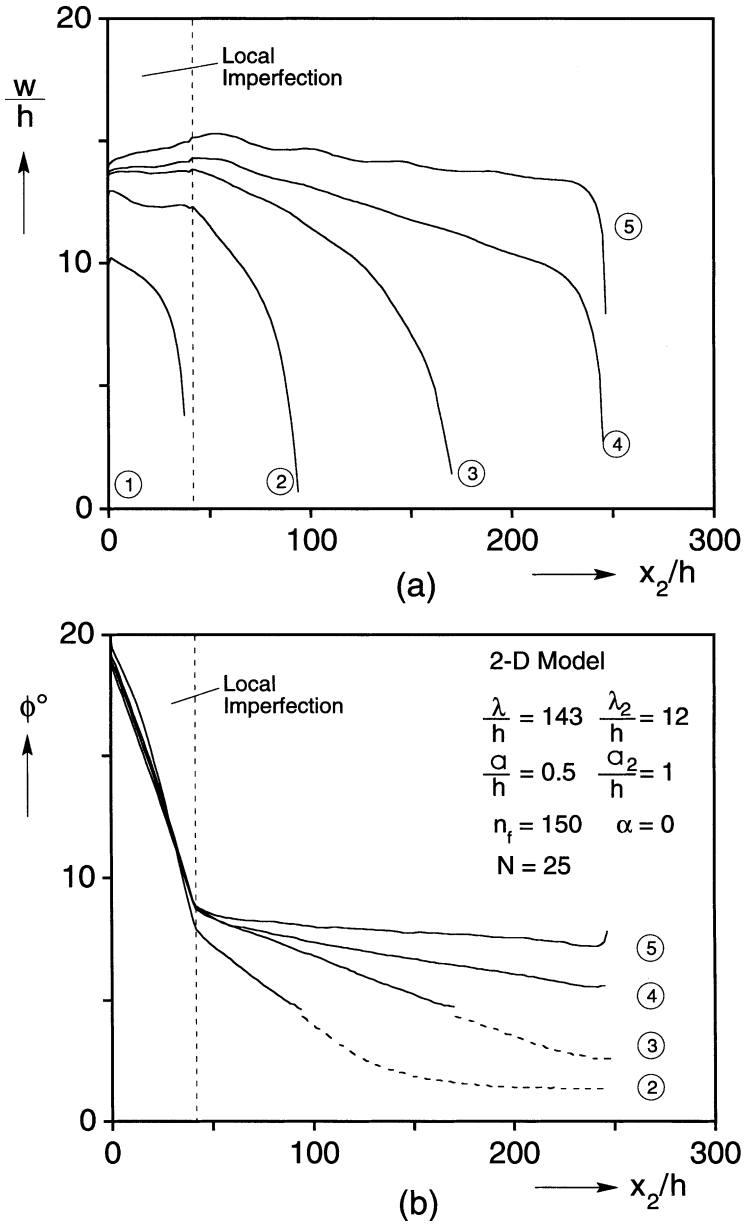

Fig. 13. Characteristics of kink band at points marked on σ_{11}–δ response in Fig. 11: (a) bandwidth and (b) fiber rotation.

somewhat for the more compliant material ($w \approx 14h$). Concurrently, the maximum rotation of the fibers inside the band decreased for the wider band and increased for the narrower one. We will see that this trend will persist for the other cases analyzed. This can be explained as follows. A fully developed kink band has associated with it a lateral deflection, v, which from geometric considerations (Fig. 5[1]) can be approximated by

$$v \cong w \sin\phi. \tag{5}$$

Table 4
Critical stresses and kink band characteristics for 2-D models with various composite parameters

v_f (%)	h μm	σ_{om} ksi	n_f	n_f	σ ksi (MPa)	τ_C ksi (MPa)	ϕ°	β°	w/h
60	7	9.5	150	12	90 (621)	7.13 (49.2)	8	5.4	16
70	7	9.5	175	12	90 (621)	7.96 (54.9)	6	5.2	18
50	7	9.5	125	12	90 (621)	6.35 (43.8)	8	5.6	14
60	3.5	9.5	300	24	60 (414)	8.44 (58.2)	11	4.9	12
60	14	9.5	75	6	90 (621)	7.42 (51.2)	5	6.4	21
60	7	14.25	150	12	90 (621)	12.2 (84.1)	9	6.0	18
60	7	4.75	150	12	90 (621)	2.36 (16.3)	6	4.9	12

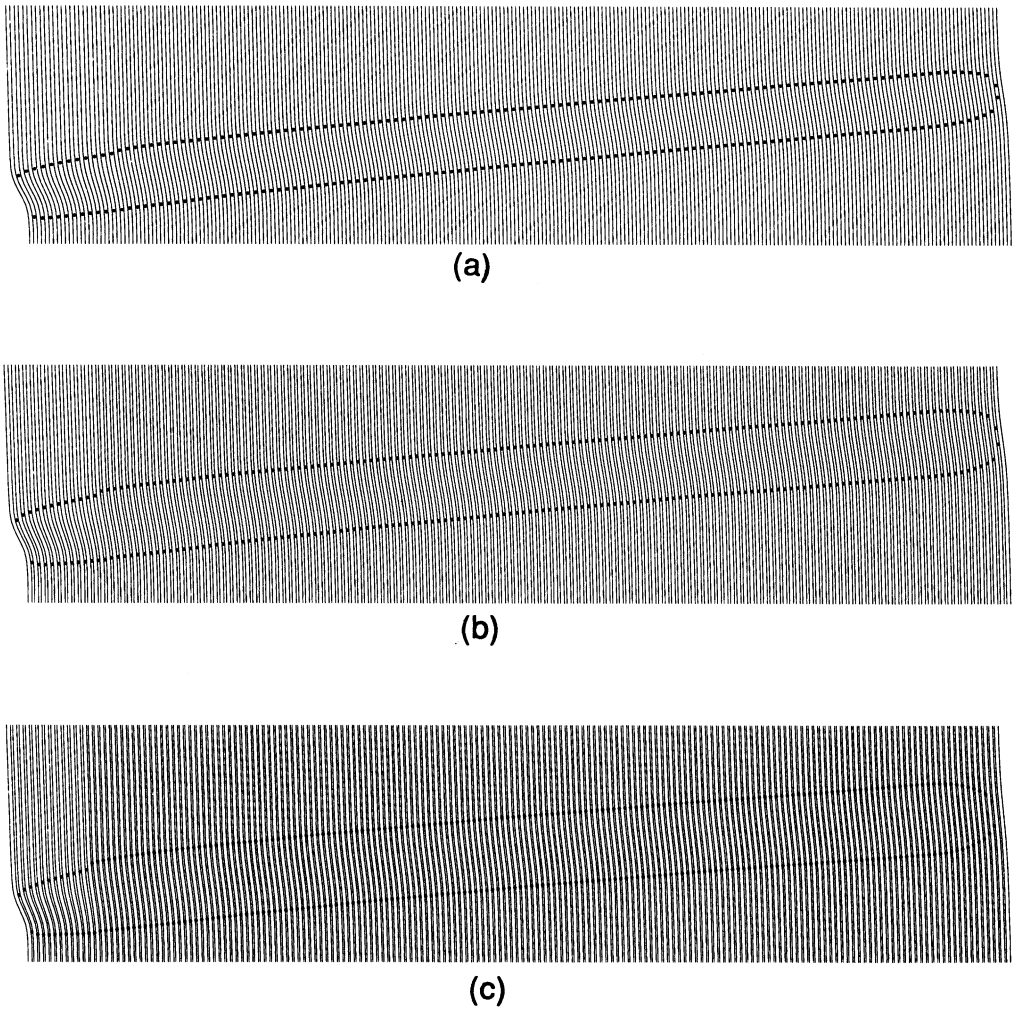

Fig. 14. Comparison of fully developed kink bands in 2-D simulations with three fiber volume fractions: (a) $v_f = 50\%$, (b) $v_f = 60\%$, and (c) $v_f = 70\%$.

In a displacement controlled situation like the one we have in the present simulations, all other variables being equal, the extent of fiber rotation is governed by the applied lateral displacement $v(\lambda)$. Comparing the change in the displacement at the initiation of the kink band (near the maximum shear stress) and when it has fully crossed the micromodel, the values of Δv are very similar for most of the cases being considered. Thus, any variable change that results in a change in the bandwidth will usually correspondingly cause a reduction in the fiber rotation ϕ.

The fiber diameter was varied next. The base case has a fiber diameter of 7 μm; in addition, we considered fibers 3.5 and 14 μm thick. Again, in order to maintain the microsection width constant, the number of fibers was respectively increased and decreased to the number given in Table 4. For the model with $h = 3.5$ μm, the initial compressive stress had to be reduced to 60 ksi as the post-failure response could not be traced until a fully developed kink band formed for 90 ksi. The main effect of altering h is that the width of fully developed kink bands is altered as shown in Fig. 15 due to the change in the effective bending rigidity of the deforming material. For $h = 7$ μm, the width of the band is $16h$. Increasing h makes the kink band wider ($w \approx 21h$), while decreasing it makes it narrower ($w \approx 12h$). Simultaneously, the fiber rotation inside the bands decreased for the thicker fibers and increased for the thinner ones for the reason given above. The band inclination decreased slightly to 4.9° for the thinner fibers and increased slightly to 6.4° for the thicker fibers.

The next variable varied was the yield stress of the matrix. Here the shape of the stress–strain response was kept unaltered (Fig. 4a) but the yield stress (σ_{om} in Table 1 Panel C) is multiplied by factors of 0.5 and 1.5, respectively. This changes the shear response of the composite with a proportionate effect on the strength. The critical shear stress decreases for the first case to 2.36 ksi (16.3 MPa) and increases for the second case to 12.2 ksi (84.1 MPa). Fig. 16 shows a comparison of three fully developed kink bands for the three matrix yield stresses. For the lower yield stress matrix, the width of the band decreases to $12h$ and the band inclination decreases slightly to 4.9°. For the higher yield stress material, the bandwidth increases to $18h$ while the band inclination increases slightly to 6°.

3.3.2. Imperfection parameters

The parameters of the local imperfection were varied next, keeping other variables constant. The amplitude of the local imperfection was reduced to $a_2 = 0.5h$. The wavelength was increased to $\lambda_2 = 24h$. The extent of the local imperfection was increased to affect 25 fibers rather than the standard 12. The results for each case are listed in Table 5. The effect on the band characteristic inclination, on its fully developed width and on the fiber rotation inside the bands is very small. Finally, the amplitude of the overall imperfection was doubled to a value of $a = h$. In this case, the critical shear stress is reduced to 6.24 ksi (43.0 MPa) and the band inclination increased slightly to 6.5°.

3.3.3. Model parameters

The effect of the width of the micromodel on the band characteristics was examined as follows. The standard model was 150 fibers wide. Models 100 and 200 fibers wide were also analyzed. The band inclination was found to increase slightly for the narrower model and to decrease slightly for the wider one (Table 5). These small changes are caused mainly by the uniform sinusoidal imperfection of the models. As the aspect ratio of the model changes, the band, because of its inclination, runs into material with different initial imperfection. When the initial fiber inclination is larger, the band inclination increases somewhat. When the fiber inclination is smaller, the band inclination decreases by a small amount.

The 2-D micromodels discussed this far were assumed to be under a state of plane stress (2-D PS in Table 3). The base case was also analyzed under plane strain assumptions. The results are summarized in the second row of Table 3 designated as 2-D PSN. The effect of this switch on the critical stress and on the band characteristics was found to be small.

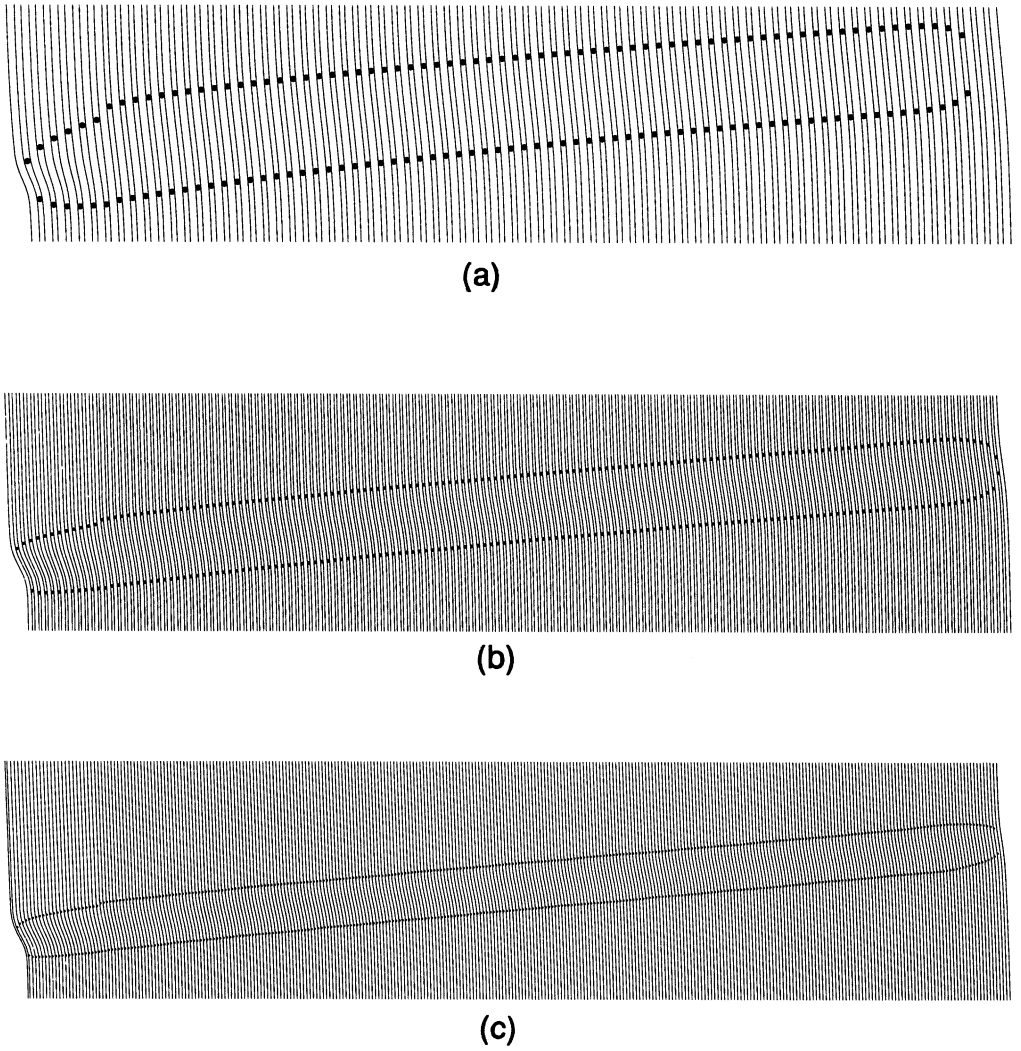

Fig. 15. Comparison of fully developed kink bands in 2-D simulations with three fiber thicknesses: (a) $h = 14$ μm, (b) $h = 7$ μm, and (c) $h = 3.5$ μm (for clarity alternating fiber–matrix boundaries omitted in (c)).

3.4. Effect of matrix dilatancy

The base case is now re-analyzed with the Drucker–Prager plasticity model (associative version) replacing the J_2 constitutive frame work used so far to model the inelastic behavior of the matrix. Guided by the results of Hsu et al. (1999b), a value of $\alpha = 0.1415$ is adopted. The results of this calculation are shown in Figs. 17–19. The average shear stress–displacement response in Fig. 17 is very similar to the corresponding results for $\alpha = 0$ in Fig. 5. The predicted critical shear stress is 7.2 ksi (49.6 MPa), a value very close to the critical stress for $\alpha = 0$ (see comparison in Table 3). The evolution of the bandwidth and the fiber rotation inside it, shown in Figs. 18 , are also very similar to the corresponding results for $\alpha = 0$ in Fig. 7. The fully developed band has a width of approximately $16h$, and the fiber rotation inside it is

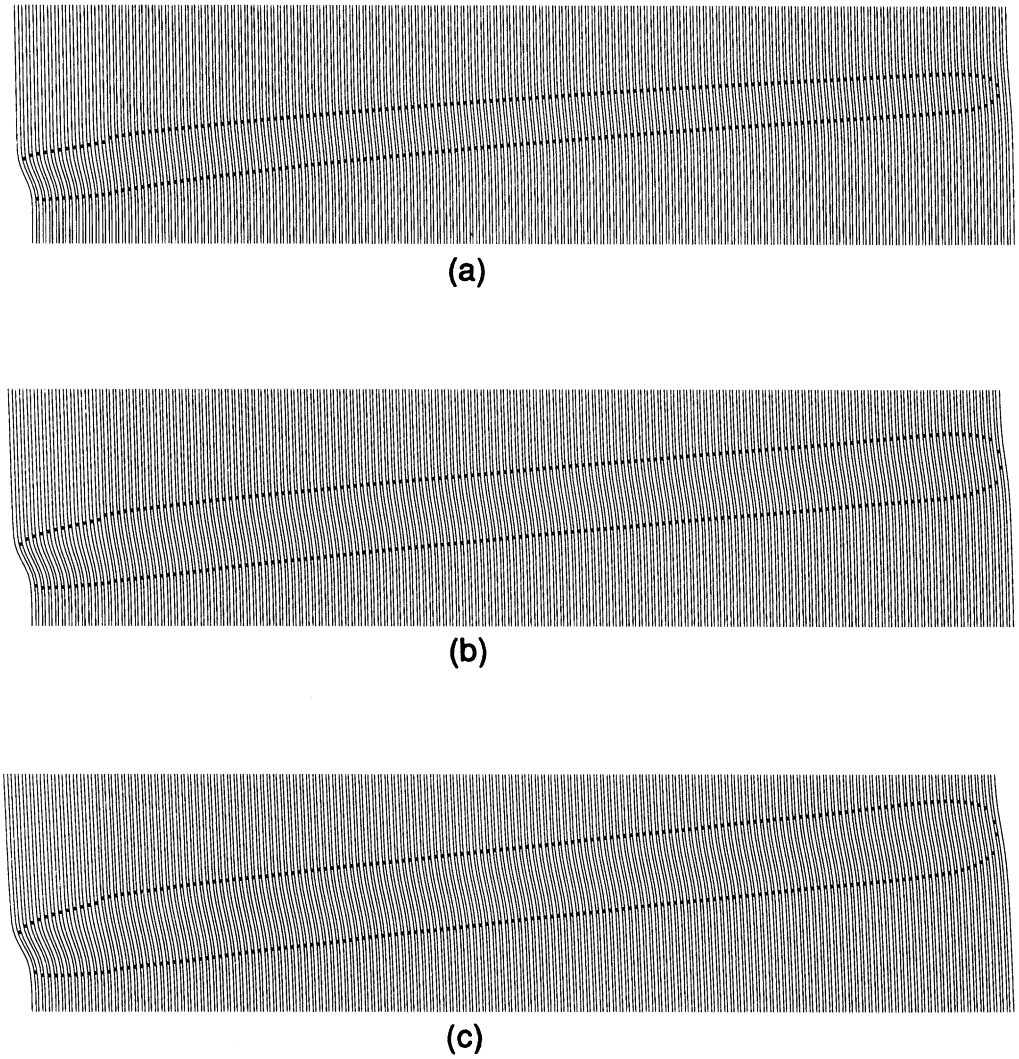

Fig. 16. Comparison of fully developed kink bands in 2-D simulations with matrix of three yield stress values: (a) $\sigma_{om} = 4.75$ ksi, (b) $\sigma_{om} = 9.5$ ksi, and (c) $\sigma_{om} = 14.25$ ksi.

Table 5
Critical stresses and kink band characteristics for 2-D models with various imperfection and model parameter

a/h	λ/h	a_2/h	λ_2/h	n_f	N	σ ksi (MPa)	τ_C ksi (MPa)	ϕ°	β°	w/h
0.5	143	1.0	12	150	12	90 (621)	7.13 (49.2)	8	5.4	16
0.5	143	0.5	12	150	12	90 (621)	7.36 (50.8)	7	5.7	15
0.5	143	1.0	24	150	12	90 (621)	7.23 (49.9)	7	4.8	15
0.5	143	1.0	12	150	25	90 (621)	6.72 (46.3)	7	5.2	16
1.0	143	1.0	12	150	12	90 (621)	6.24 (43.0)	7	6.5	16
0.5	143	1.0	12	100	12	90 (621)	7.12 (49.1)	7	6.1	14
0.5	143	1.0	12	200	12	90 (621)	7.30 (50.3)	7	4.9	16

approximately 8°. Fig. 19 shows several deformed configurations of the truncated microsection, which illustrate the evolution of the band as it crosses the specimen. A striking difference between these configurations and those in Fig. 6 is that the inclination of the band is now approximately 10.2° or nearly double its value for $\alpha = 0$.

This strong sensitivity of the band inclination to matrix compressibility was confirmed in a series of additional calculations in which the value of α was varied. The results are summarized in Fig. 20 where the

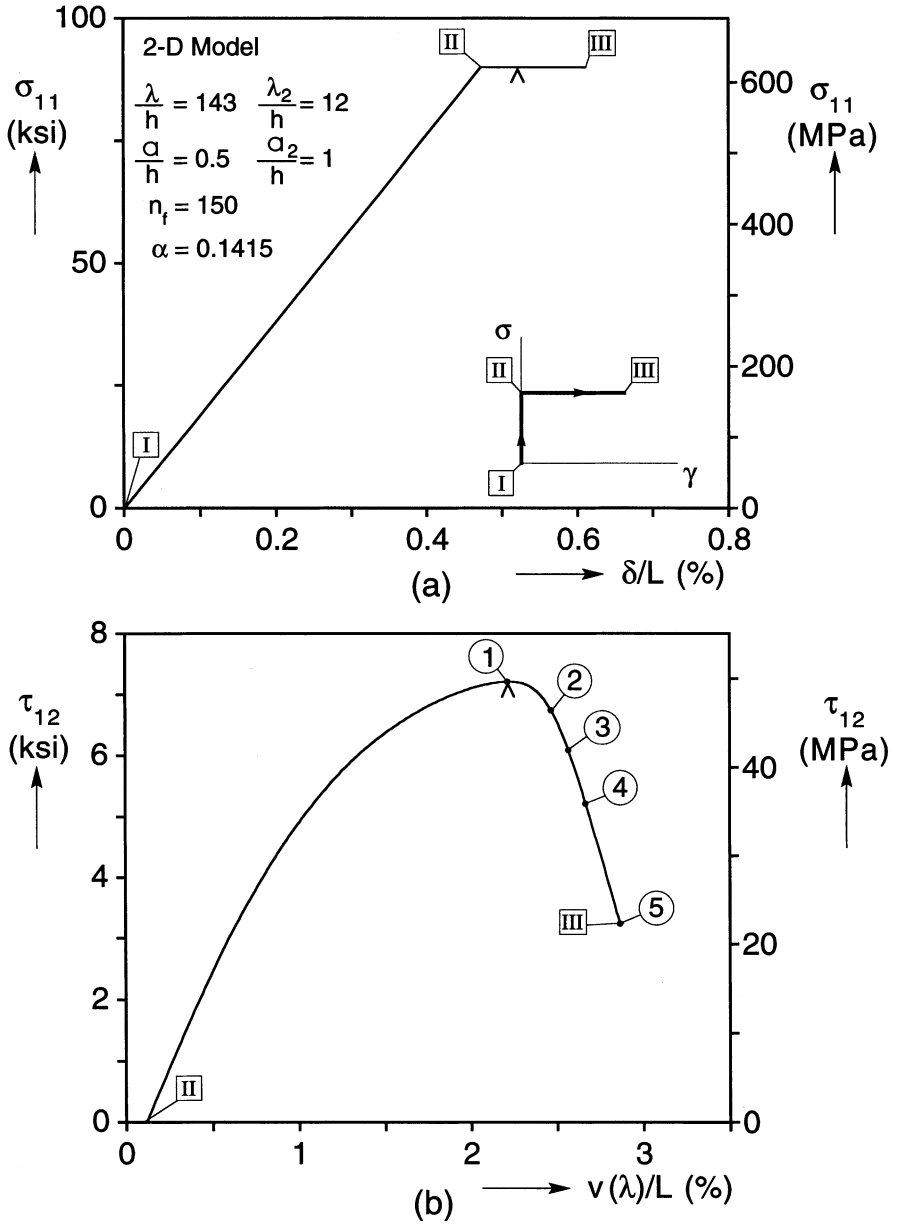

Fig. 17. Results from the 2-D model using Drucker–Prager model for matrix. (a) axial stress-end shortening and (b) shear stress–horizontal displacement responses.

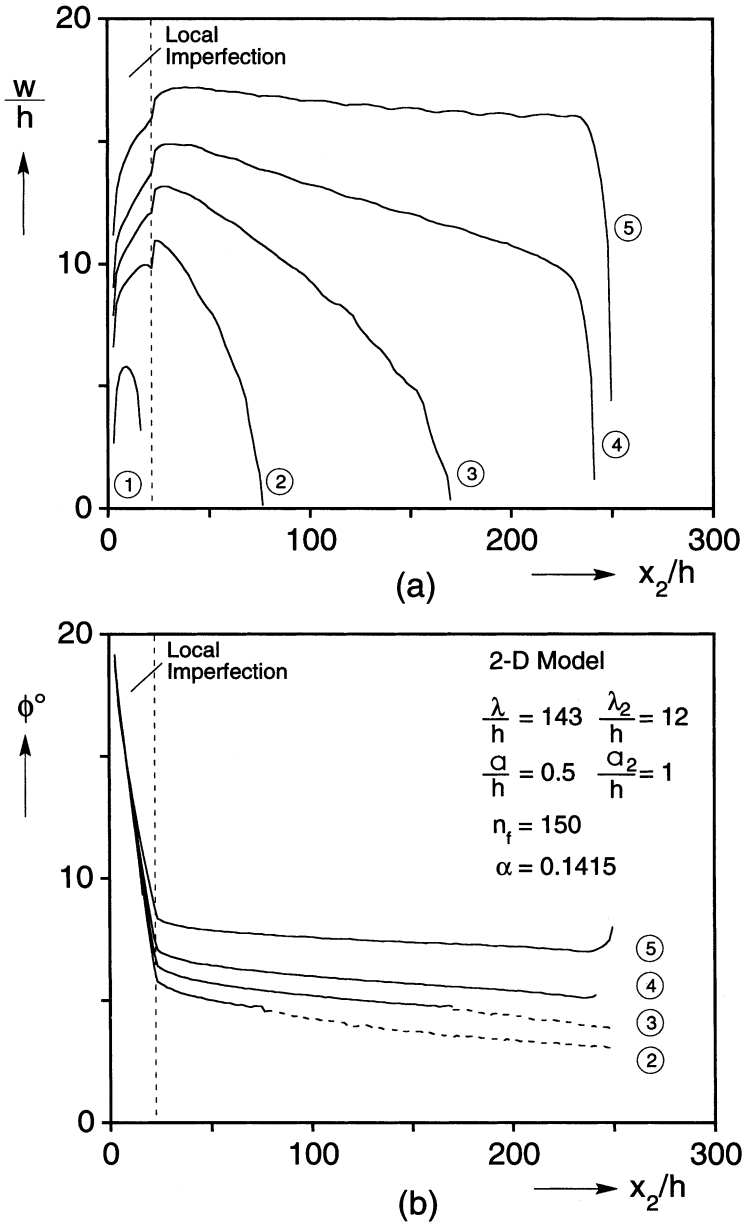

Fig. 18. Characteristics of kink band at points marked on τ_{12}–$v(\lambda)$ response in Fig. 17b. (a) bandwidth and (b) fiber rotation.

band inclination is seen to increase linearly with α starting at 5.4° for $\alpha = 0$ and ending up at nearly 12.4° for $\alpha = 0.192$. It is important to point out that the main effect of the D–P model is in the inclination of the growing band, a post-failure event. The onset of failure is still mainly governed by the shear response of the composite which is not affected significantly by α. Once failure starts and the band starts to grow, inside the band there are two main deformation mechanisms. First, the material is sheared by an amount closely approximated by the fiber rotation angle ϕ (Budiansky and Fleck, 1993)[1]. As pointed out, the shear

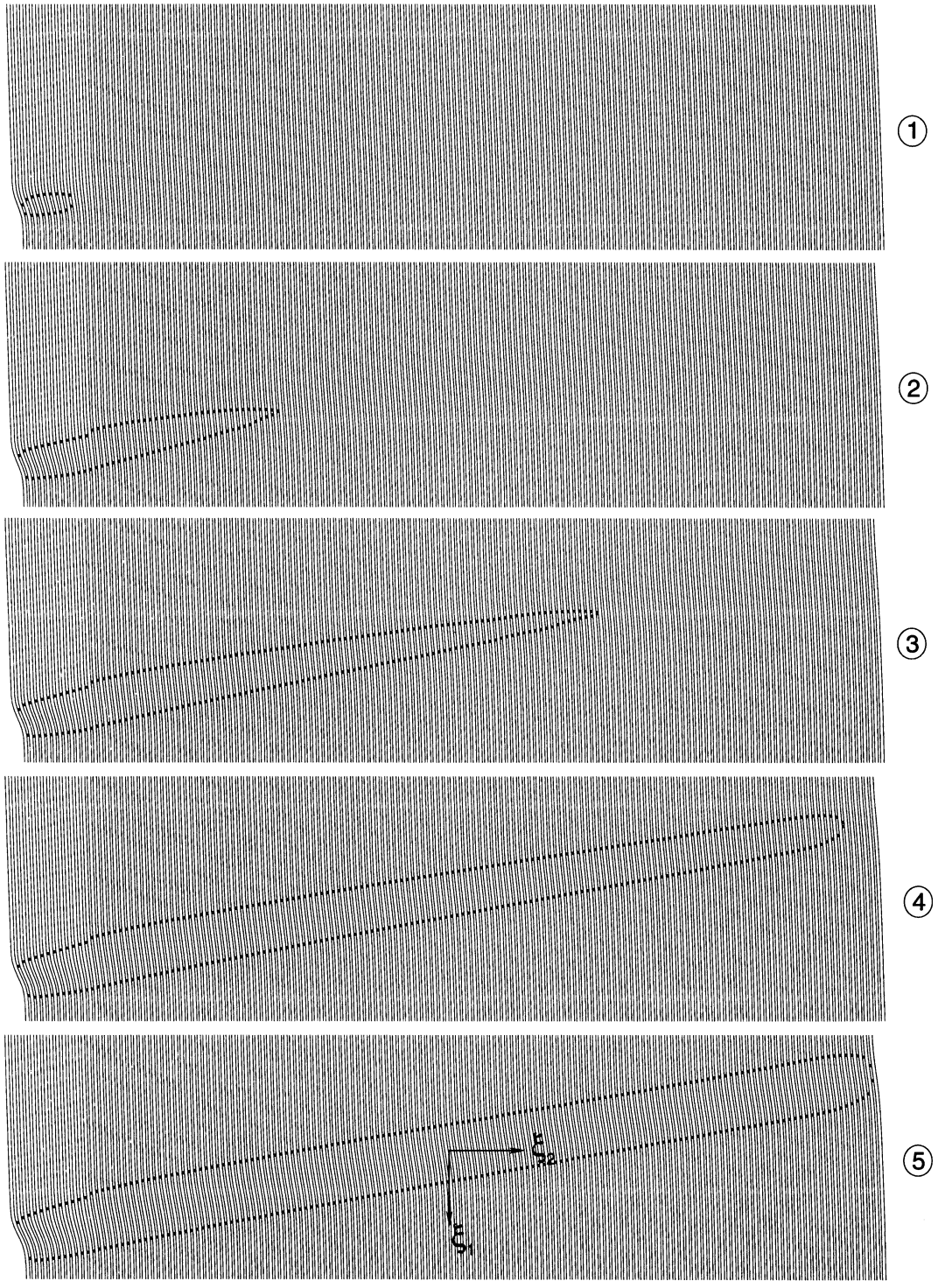

Fig. 19. Truncated deformed configurations of the 2-D model showing growth of kink band across it. Configurations correspond to points marked on τ_{12}–$\nu(\lambda)$ response in Fig. 17b.

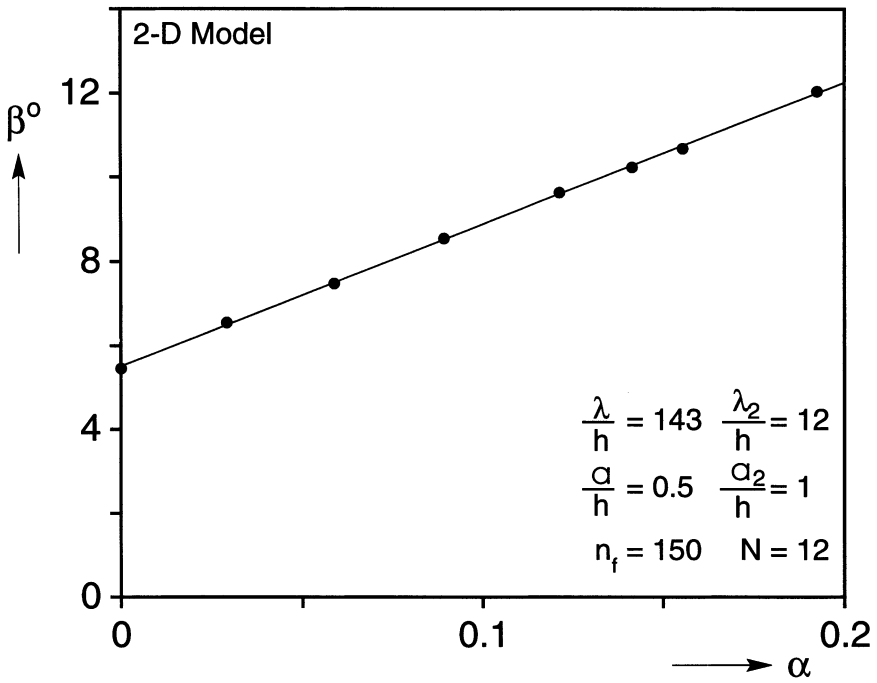

Fig. 20. Predicted kink band inclination β for various values of α in the D-P model.

response of the material is not altered by α, and the shear stress and strain distribution inside the band remain unaltered. The second deformation mechanism is straining transverse to the fibers. If we adopt the simplifying assumptions of Budiansky and Fleck (1993)[1] that the strain along the fibers is negligibly small, then the transverse strain is given by

$$\varepsilon_T = \ln\left[\frac{\cos(\beta - \phi)}{\cos\beta}\right]. \tag{6}$$

Furthermore, to first order, ε_T also corresponds to the volumetric strain. Fig. 21 shows a comparison of profiles of strain transverse to the rotated fibers for $\alpha = 0$ and $\alpha = 0.1415$. The strains are plotted along the local coordinate ξ_1 (Figs. 6 and 19). Clearly, the dilatation of the matrix allowed by the D–P model results in the development of higher transverse tension in the matrix in the early stages of its formation. If we accept that the fiber rotation angle inside the forming band is approximately the same for the two values of α (Figs. 7b and 18b), Eq. (6) clearly implies that a higher value of ε_T will result in a larger value of the band inclination β. Indeed, in the range of values of the three variables of interest, for fixed values of ϕ in Eq. (6), the angle β varies linearly with ε_T. Since ε_T is linearly related to α, the linear dependence of β to α seen in Fig. 20 follows.

The 3-D model was also run using the D–P model for the matrix. The results of such a simulation are summarized in Table 3. The band inclination increased even further to 17.3°. We suspect that the more complex 3-D microstructure provides even higher constraint to the matrix in the deforming band and a correspondingly higher β. The predicted value is higher than the 12–13° observed in the compression–shear experiments discussed in Part I. This, perhaps, is another indication that the D–P model does not capture with accuracy all complexities of in situ PEEK nonlinearities.

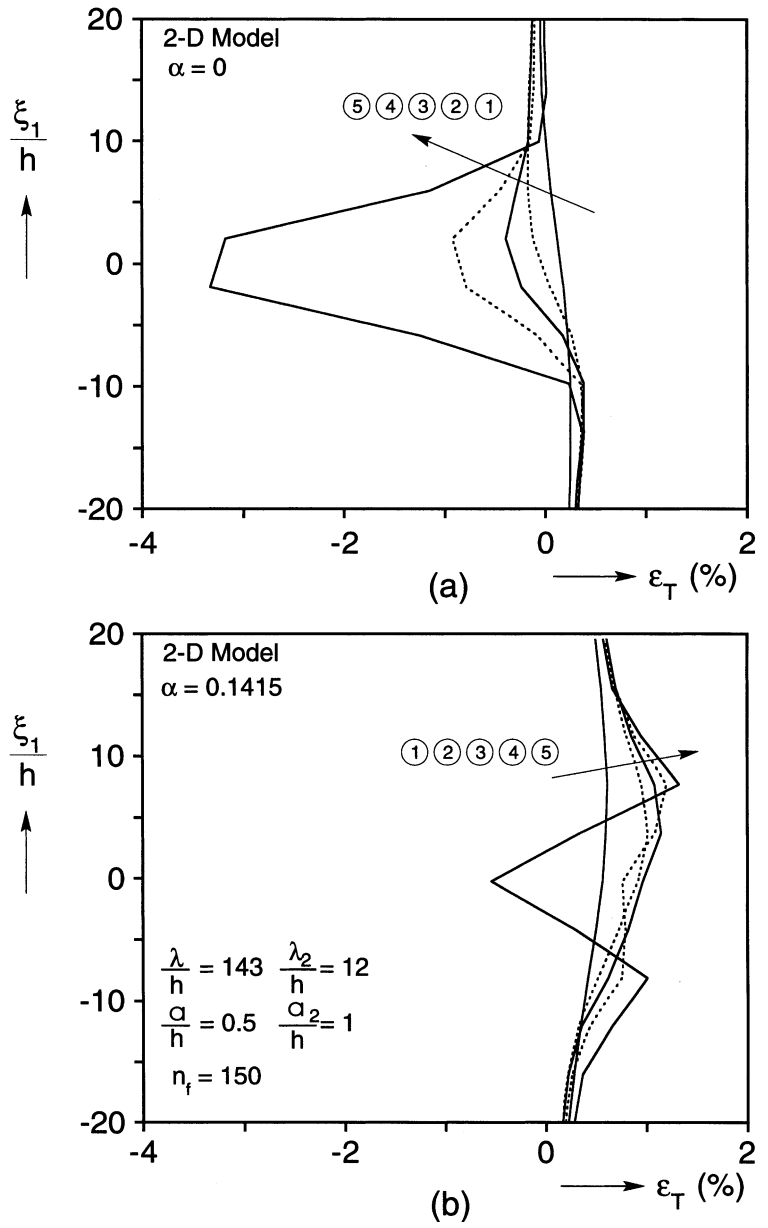

Fig. 21. Evolution of transverse strain ε_T inside kink band for (a) $\alpha = 0$ and (b) $\alpha = 0.1415$.

It was interesting to repeat the 2-D simulation with $\alpha = 0.1415$ under plane strain conditions. The results are summarized in Table 3. In this case also, the additional constraint increased to some degree the critical stress but, more importantly, pushed the inclination of the fully developed band to 14.6°.

Finally, we repeated the 2-D pure compression simulation using the D–P model. The results are compared to those of J_2 plasticity in Table 6. As expected, the effect of the model on the critical stress was relatively small causing an increase of only 2.5%. Because of the high stiffness of the fibers, the net pressure that builds up in the matrix is relatively small before the limit load is reached. Thus, the shear response

Table 6
Critical stresses and kink band characteristics for 2-D microsections loaded under pure compression

α	N	σ_C ksi (GPa)	ϕ°	β°	w/h
0	25	192 (1.32)	8	4.8	15
0.1415	25	197 (1.36)	8	10.1	15

remains relatively unchanged which reflects on the relatively small change in the limit stress. By contrast, the kink band inclination increased to approximately 10.1°, a value comparable to that in Table 3 for the compression–shear simulation.

4. Conclusions

Previously, we developed, calibrated and used 2-D and 3-D micromechanical models of unidirectional composites to study the onset of failure due to compression and the evolution of post-failure events (Kyriakides et al., 1995,[1] Hsu et al., 1998,[1] 1999a). Failure was found to be associated with a limit load instability governed by the interaction of the nonlinear shear response of the material with small fiber misalignments present in the composite (Argon, 1972;[1] Budiansky, 1983[1]). Following the limit load, deformation is localized in bands of highly bent fibers. The geometric imperfections used in these studies were primarily global in nature and, as a result, from their onset the bands extended across the width of the finite size models. The bands started essentially with zero inclination but, as the fiber bending and rotation inside them increased, they became more inclined.

In the present work, in order to capture how such bands initiate locally and grow across the composite, local imperfections were added to a free edge of the model. In addition, following the experimental findings of Part I, the alternate problem of failure due to compression followed by shear was examined as it provides a more hospitable setting for tracing the post-failure events than pure compression loading. It has been found that, under displacement controlled shearing, local fiber buckling initiates from the local imperfection in the process leading to a limit load in the applied shear. The buckled fibers bend and rotate, emanating a "characteristic" which quickly spreads into the essentially intact material across the model. Subsequently, localized fiber buckling grows along this "characteristic" direction. In essence, the front of the growing band provides the destabilizing shear deformation for the material ahead of it, so that the band too can grow. Thus, the gradual development of a band in models of uniform imperfection, starting from zero inclination at the limit load and growing to an inclined band with a distinct width, can be viewed as the sequence of events that take place in the transition zone in the tip of the growing band.

Although the main thrust of the study involved compression–shear loading, models loaded in pure compression were also analyzed. Provided the local imperfection was sufficiently large, it was possible to initiate and grow inclined kink bands across the models. The cusp-like post-failure response for this loading makes tracing the kink band more difficult but, for the cases examined, the characteristics of the growing inclined kink bands were similar to those seen for compression–shear loadings.

The characteristics of kink bands initiated from a local imperfection and allowed to grow across the model were studied parametrically using both 2-D and 3-D models. At first, the PEEK matrix was represented as a J_2 elasto-plastic solid. This model was shown in the past to be quite adequate for calculating accurately the onset of failure. The following trends were established:

- Once a kink band was initiated, its evolution across the microsection resembled experimental observations. The calculated bandwidths were comparable to measured values whereas the band inclinations were uniformly on the order of one-half experimentally observed values of β.

- The kink band width increased/decreased with the fiber diameter and to a lesser extent with the fiber volume fraction. It also increased/decreased with the yield stress of the matrix. By contrast, β was relatively insensitive to these variables.
- The amplitude, length, and extent of the local imperfection were varied and, within the range of this variation, no significant effect on the characteristics of kink bands was observed. The same general insensitivity was found when the amplitude of the global imperfection was varied.
- The width of the microsection was also varied and, again, for the range of values examined, the band characteristics changed very modestly.
- Kink bands developed in plane stress and plane strain models were compared and their general characteristics were found to be similar.
- Despite the more complex microstructure of 3-D models, the overall characteristics of predicted kink bands were similar to those of "corresponding" 2-D models.

Previous investigations demonstrated that the nonlinearities of AS4/PEEK are complicated by inelastic dilatancy and sensitivity to hydrostatic pressure. The Drucker–Prager model provides a simple framework for incorporating aspects of this pressure sensitivity of the material (albeit, as shown in Hsu et al. (1999b) not completely accurately). It was thus adopted in order to enable investigation of the sensitivity of the solution to variables not available in J_2 plasticity.

The shear response of the composite is essentially unaffected by the switch to this model. Thus, the responses of the micromodels up to the onset of failure were essentially unaltered by the D–P model. The effect of the model was felt strongly in the post-failure events where, for all cases examined, the kink band inclination increased significantly from the value predicted for the corresponding case using J_2 plasticity. The increase in β was even more pronounced for the 3-D model and for 2-D plane strain calculations, due to the more constrained setting they provide to the growing band. Finally, a parametric study demonstrated that the calculated band inclination is proportional to the D–P parameter α. Clearly, prediction of kink band inclinations requires matrix models which accurately capture its sensitivity to pressure and its dilatancy.

Acknowledgements

The financial support of the Ship Structures and Systems Division of the Office of Naval Research, Dr. Y.D.S. Rajapakse program director, through grant no. N00014-00-1-0585 is acknowledged with thanks. T.J.V. and S.Y.H. wish to thank the University of Texas at Austin for additional support provided to them in the course of this study. Computing resources were also provided by the National Partnership for Advanced Computational Infrastructure at the San Diego Supercomputer via the NSF cooperative agreement ACI-9619020.

References

Christiansen, A.W., Baer, E., Radcliffe, S.V., 1971. The mechanical behavior of polymers under high pressure. Philosophical Magazine 24, 451–467.

Drucker, D., Prager, W., 1952. Soil mechanics and plastic analysis for limit design. Quarterly of Applied Mathematics 10, 157–165.

Hsu, S.-Y., Vogler, T.J., Kyriakides, S., 1999a. On the axial propagation of kink bands in fiber composites: Part II. Analysis. International Journal of Solids and Structures 36, 575–595.

Hsu, S.-Y., Vogler, T.J., Kyriakides, S., 1999b. Inelastic behavior of an AS4/PEEK composite under combined transverse compression and shear: Part II Analysis. International Journal of Plasticity 36, 575–595.

Pixa, R., Le Du, V., Wippler, C., 1988. Dilatometric study of deformation induced volume increase and recovery in rigid PVC. Colloid and Polymer Science 266, 913–920.

Santore, M.M., Duran, R.S., McKenna, G.B., 1991. Volume recovery in epoxy glasses subjected to torsional deformations: the question of rejuvenation. Polymer 32, 2377–2381.

Sauer, J.A., Pae, K.D., Bhateja, S.K., 1973. Influence of pressure on yield and fracture in polymers. Journal of Macromolecular Science – Physics B8, 631–654.

Spitzig, W.A., Richmond, O., 1979. Effect of hydrostatic pressure on the deformation behavior of polyethylene and polycarbonate in tension and in compression. Polymer Engineering and Science 19, 1129–1139.